

# Proceedings of the Institution of Mechanical Engineers, Part A: Journal of Power and Energy

<http://pia.sagepub.com/>

---

## Similitude and scaling laws for the rotating flow between concentric discs

Abhijit Guha and Sayantan Sengupta

*Proceedings of the Institution of Mechanical Engineers, Part A: Journal of Power and Energy* 2014 228: 429 originally

published online 10 March 2014

DOI: 10.1177/0957650914523947

The online version of this article can be found at:

<http://pia.sagepub.com/content/228/4/429>

---

Published by:



<http://www.sagepublications.com>

On behalf of:



[Institution of Mechanical Engineers](http://www.imeche.org)

Additional services and information for *Proceedings of the Institution of Mechanical Engineers, Part A: Journal of Power and Energy* can be found at:

**Email Alerts:** <http://pia.sagepub.com/cgi/alerts>

**Subscriptions:** <http://pia.sagepub.com/subscriptions>

**Reprints:** <http://www.sagepub.com/journalsReprints.nav>

**Permissions:** <http://www.sagepub.com/journalsPermissions.nav>

**Citations:** <http://pia.sagepub.com/content/228/4/429.refs.html>

>> [Version of Record](#) - Apr 29, 2014

[OnlineFirst Version of Record](#) - Mar 10, 2014

[What is This?](#)

# Similitude and scaling laws for the rotating flow between concentric discs

Proc IMechE Part A:  
J Power and Energy  
2014, Vol. 228(4) 429–439  
© IMechE 2014  
Reprints and permissions:  
sagepub.co.uk/journalsPermissions.nav  
DOI: 10.1177/0957650914523947  
pia.sagepub.com



Abhijit Guha and Sayantan Sengupta

## Abstract

In this article, a systematic dimensional analysis and similitude study for the three-dimensional rotating flow within the narrow spacing (usually of the order of 100  $\mu\text{m}$ ) of multiple concentric discs is presented. An engineering application of this flow configuration is the Tesla disc turbine, and the dimensional analysis leads to proper scaling laws for such machines. Using the Buckingham Pi theorem, the list of non-dimensional numbers necessary for describing the incompressible flow through the concentric discs has been formulated and physical interpretation of the non-dimensional numbers has been provided. The complete criteria for achieving geometric, kinematic and dynamic similarity between a model and the prototype have been established. Computational fluid dynamics (CFD) solutions have been obtained for various geometries, fluid properties and flow conditions to demonstrate the validity of the similitude criteria developed. The CFD results show that, when the present similitude criteria are fulfilled, the values of all non-dimensional output parameters such as the power and pressure-drop coefficients remain unchanged for various combinations of input variables. What is more striking is that the three-dimensional variations of non-dimensional  $z$  component of velocity  $U_z$  (whose non-zero values are computed by the CFD solver even though the only physical boundary condition applied is  $U_z = 0$  at the inlet and on disc surfaces) are superposed on one another for all models and the prototype. Systematic methods for arriving at simplified conservation equations are discussed and it is shown how the corresponding list of non-dimensional numbers and similitude criteria evolve with such simplification of the conservation equations.

## Keywords

Tesla disc turbine and compressor, non-dimensional numbers, scaling laws, rotating flow, 3-D CFD simulation

Date received: 2 September 2013; accepted: 7 January 2014

## Introduction

According to Dixon and Hall,<sup>1</sup> dimensional analysis enables one to predict the behaviour of the prototype from that of a model, to determine the most suitable machine for a particular operating condition or to reduce the experimental effort in determining functional relationships between flow variables. In this article, a systematic dimensional analysis for the three-dimensional rotating flow within the narrow spacing (usually of the order of 100  $\mu\text{m}$ ) of multiple concentric discs is provided. Fluid flow within a Tesla disc turbine represents such a flow scenario.

Tesla turbine was invented by the famous scientist Nikola Tesla in 1913.<sup>2</sup> Unlike a conventional bladed turbine, the rotor of a Tesla turbine is formed by a series of flat, parallel, co-rotating discs which are closely-spaced and attached to a central shaft. The working fluid is injected nearly tangentially to the rotor by

means of one or more inlet nozzles. The injected fluid, which passes through the narrow gaps between the discs, approaches spirally towards the exhaust port located at the centre of each disc. The viscous drag force, which is generally considered to be a source of loss for conventional turbine, causes the rotor of the disc turbine to rotate. There is a housing surrounding the rotor, with a small radial and axial clearance. Figure 1 shows a schematic of two successive discs of the rotor of a Tesla turbine. The components of the velocity at the inlet are represented by arrows. For a

---

Mechanical Engineering Department, Indian Institute of Technology Kharagpur, Kharagpur, India

### Corresponding author:

Abhijit Guha, Mechanical Engineering Department, Indian Institute of Technology Kharagpur, Kharagpur 721302, India.  
Email: a.guha@mech.iitkgp.ernet.in

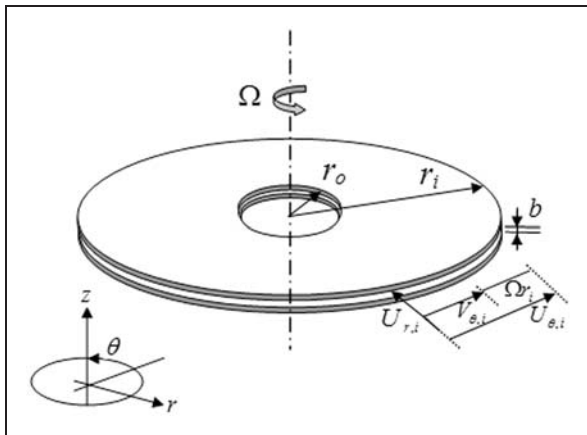


**Figure 1.** Schematic diagram of the domain for the mathematical solution. (The gap within the two discs, in relation to the radius, is exaggerated in the sketch for clarity.)

Tesla turbomachine, subjected to a steady rotational speed  $\Omega$ , the components of absolute velocity ( $r$ ,  $z$  and  $\theta$  components of  $U$ ) are related to the components of relative velocity ( $r$ ,  $z$  and  $\theta$  components of  $V$ ) by the following transformation:

$$U_r = V_r; \quad U_z = V_z; \quad U_\theta = (V_\theta + \Omega r) \quad (1)$$

After the success of Whittle and von Ohain, the gas turbine became the centrepoint of research and development and the understanding of its performance and optimization has reached quite a mature stage (Guha<sup>3,4</sup>). The understanding of the performance of Tesla turbines is not nearly as thorough. Rice<sup>5</sup> in his article had described the advances (upto 1991) in the field of Tesla turbomachinery (pump, fan and turbine). Experimental and theoretical studies in this field are still being reported. Lemma et al.,<sup>6</sup> Hoya and Guha<sup>7</sup> and Guha and Smiley<sup>8</sup> had performed detailed experiments with Tesla disc turbines. A simple but very effective method for measuring the net power output and overall loss (the bearing and other losses), called the “angular acceleration method”, has been developed and fully described by Hoya and Guha.<sup>7</sup> This is a successful method for measuring very low torque at very high angular speed. The reference also provides detailed measurements and operational experience for Tesla disc turbines. Guha and Smiley<sup>8</sup> have developed an improved design of the nozzle, greatly improving the efficiency and achieving uniformity in the velocity profile of the jet. [The loss in the nozzle is generally recognized (Rice<sup>5,9</sup>) as a major source of loss in a conventional Tesla turbine.] Recent advancement in theoretical study of Tesla disc turbine can be found in Carey,<sup>10</sup> Sengupta and Guha<sup>11</sup> and Guha and Sengupta.<sup>12</sup> Carey<sup>10</sup> developed a one-dimensional idealized

momentum transfer model of Tesla turbine. Sengupta and Guha<sup>11</sup> have developed closed-form analytical solution for three-dimensional axi-symmetric flow fields inside the narrow disc-gap of a Tesla disc turbine (considering cylindrical co-ordinate system in a relative rotational frame of reference). Guha and Sengupta<sup>12</sup> have shown how the dynamics of fluid flow between the two discs of a Tesla turbine is governed by the centrifugal, Coriolis, viscous and inertial components of force.

The rotor of some other devices, e.g. rotating air cleaner,<sup>13</sup> is also composed of multiple parallel, concentric discs. However, the Tesla turbine is a power-producing device and the gap between two adjacent discs is small, which may be small enough in certain cases to be considered as a micro-channel. Usually the two boundary layers on the two discs would merge together, so that a core flow of the Batchelor-type<sup>14</sup> does not occur.

The Tesla disc turbine has several advantages, one of them is that a variety of working fluids may be used. Other than the usual fluids such as air, steam and water, two phase mixture (many aspects of two-phase flow may be found in Guha<sup>15-19</sup>) such as biomass fuel has also been used by previous researchers.<sup>20</sup> Tesla turbine was also used to generate power in geothermal power stations.<sup>21</sup> A review of the literature shows that Tesla turbines of various length scales have been used by the previous researchers. Starting from Tesla,<sup>2</sup> some of the researchers like Armstrong,<sup>22</sup> and Beans<sup>23</sup> had used large scale Tesla turbines ( $r_i = 228.6$  mm in Tesla<sup>2</sup>,  $r_i = 88.9$  mm in Armstrong<sup>22</sup> and  $r_i = 76.2$  mm in Beans<sup>23</sup>). On the other hand, Davydov and Sherstyuk,<sup>24</sup> and Lemma et al.<sup>6</sup> had used Tesla turbines of small size ( $r_i = 20$  mm in Davydov and Sherstyuk<sup>24</sup> and  $r_i = 25$  mm in Lemma et al.<sup>6</sup>). Hoya and Guha<sup>7</sup> and Guha and Smiley<sup>8</sup> had used a Tesla turbine of intermediate size ( $r_i = 46$  mm in both Hoya and Guha<sup>7</sup> Guha and Smiley<sup>8</sup>). It is clear from the above discussion that there is a real need for a proper dimensional analysis to determine the most suitable Tesla turbine for a particular situation. However, as per our knowledge there is no article available in the literature which describes the dimensional analysis of a Tesla disc turbine in details.

The present work formulates the appropriate non-dimensional numbers which can be used to design a Tesla disc turbine or to explain the flow physics of the rotating flow within the narrow spacing of multiple concentric discs. The criteria for achieving similitude between a model and the prototype, and appropriate scaling laws have been established. It is shown that proper non-dimensionalization and order of magnitude analysis lead to simplification of the conservation equations for which closed-form solution can be obtained. The validity of the principle of similitude formulated here has been demonstrated by several three-dimensional computational fluid dynamics (CFD) simulations.

### Dimensional analysis and criteria for similitude

#### Fundamental conservation equations

In this section, a dimensional analysis for the three-dimensional rotating flow within the narrow spacing of multiple concentric discs is provided. The present analysis is also applicable for a Tesla turbine. The domain for mathematical solutions is represented in Figure 1. The analysis starts with Navier-Stokes equations in cylindrical coordinate system for steady, incompressible flow of a Newtonian fluid with constant density and viscosity.

$$\frac{1}{r} \frac{\partial (rU_r)}{\partial r} + \frac{1}{r} \frac{\partial U_\theta}{\partial \theta} + \frac{\partial U_z}{\partial z} = 0 \tag{2}$$

$$\begin{aligned} &\rho \left( U_r \frac{\partial U_r}{\partial r} + \frac{U_\theta}{r} \frac{\partial U_r}{\partial \theta} - \frac{U_\theta^2}{r} + U_z \frac{\partial U_r}{\partial z} \right) \\ &= -\frac{\partial p}{\partial r} + \rho g_r \\ &\quad + \mu \left[ \frac{1}{r} \frac{\partial}{\partial r} \left( r \frac{\partial U_r}{\partial r} \right) - \frac{U_r}{r^2} + \frac{1}{r^2} \frac{\partial^2 U_r}{\partial \theta^2} - \frac{2}{r^2} \frac{\partial U_\theta}{\partial \theta} + \frac{\partial^2 U_r}{\partial z^2} \right] \end{aligned} \tag{3}$$

$$\begin{aligned} &\rho \left( U_r \frac{\partial U_\theta}{\partial r} + \frac{U_\theta}{r} \frac{\partial U_\theta}{\partial \theta} + \frac{U_r U_\theta}{r} + U_z \frac{\partial U_\theta}{\partial z} \right) \\ &= -\frac{1}{r} \frac{\partial p}{\partial \theta} + \rho g_\theta \\ &\quad + \mu \left[ \frac{1}{r} \frac{\partial}{\partial r} \left( r \frac{\partial U_\theta}{\partial r} \right) - \frac{U_\theta}{r^2} + \frac{1}{r^2} \frac{\partial^2 U_\theta}{\partial \theta^2} + \frac{2}{r^2} \frac{\partial U_r}{\partial \theta} + \frac{\partial^2 U_\theta}{\partial z^2} \right] \end{aligned} \tag{4}$$

$$\begin{aligned} &\rho \left( U_r \frac{\partial U_z}{\partial r} + \frac{U_\theta}{r} \frac{\partial U_z}{\partial \theta} + U_z \frac{\partial U_z}{\partial z} \right) \\ &= -\frac{\partial p}{\partial z} + \rho g_z + \mu \left[ \frac{1}{r} \frac{\partial}{\partial r} \left( r \frac{\partial U_z}{\partial r} \right) + \frac{1}{r^2} \frac{\partial^2 U_z}{\partial \theta^2} + \frac{\partial^2 U_z}{\partial z^2} \right] \end{aligned} \tag{5}$$

#### Appropriate non-dimensional numbers

Equations (2) to (5) are in dimensional form. In order to turn these equations into appropriate non-dimensional forms, a formal dimensional analysis using the Buckingham Pi theorem has been performed in Appendix 2. This analysis identifies seven non-dimensional numbers or Pi-terms. Instead of using these Pi-terms directly, we have recombined them in various manners to construct seven other non-dimensional terms for each of which a direct physical interpretation can be ascribed. These newly derived non-dimensional numbers and their relations with the original Pi-terms have been described below.

1. Radius ratio:

$$\hat{r}_o = \Pi_2 = \frac{r_o}{r_i} \tag{6}$$

2. Aspect ratio:

$$\hat{b} = \Pi_3 = \frac{b}{r_i} \tag{7}$$

3. Tangential speed ratio at inlet:

$$\gamma = \frac{\Pi_5}{\Pi_6} = \frac{\bar{U}_{\theta,i}}{\Omega r_i} \tag{8}$$

4. Flow angle at inlet:

$$\alpha = \tan^{-1}(1/\Pi_5) = \tan^{-1} \left| \frac{\bar{U}_{r,i}}{\bar{U}_{\theta,i}} \right| \tag{9}$$

5. Dynamic similarity number:

$$D_s = \frac{\Pi_3^2}{\Pi_7} = \frac{b}{r_i} \left( \frac{|\bar{U}_{r,i}| b}{\nu} \right) \tag{10}$$

6. Power coefficient:

$$\hat{W} = \Pi_1 = \frac{\dot{W}}{(\rho |\bar{U}_{r,i}|^3 r_i^2)} \tag{11}$$

7. Pressure-drop coefficient:

$$\Delta \hat{p}_{io} = \frac{\Pi_4}{\Pi_5^2} = \frac{\Delta p_{io}}{\rho \bar{U}_{\theta,i}^2} \tag{12}$$

#### Criteria for similitude

For geometric similarity between the model tested and the prototype to be designed, the radius ratio  $\hat{r}_o$  and aspect ratio  $\hat{b}$  of the model should be the same as that of the prototype. For kinematic similarity between a geometrically similar model and the prototype, the tangential speed ratio at inlet  $\gamma$  and the flow angle at inlet  $\alpha$  of the model should be the same as those of the prototype. After achieving both geometric and kinematic similarity, the attainment of dynamic similarity further requires that the dynamic similarity number  $D_s$  used for the model should be the same as that of the prototype. When dynamic similarity is achieved, the principle of similitude enunciates that the power coefficient  $\hat{W}$  and the pressure-drop coefficient  $\Delta \hat{p}_{io}$  of a model would be the same as those of the prototype. Later in the paper, we have tested the principle of similitude by determining the power and pressure-drop coefficients for widely different geometries, fluids and flow conditions with the help of CFD.

### Non-dimensional conservation equations and boundary conditions

Equations (2) to (5) are non-dimensionalized using the following non-dimensional variables:

$$\hat{r} = \frac{r}{r_i}, \quad \hat{z} = \frac{z}{b}, \quad \hat{U}_\theta = \frac{U_\theta}{\Omega r_i}, \quad \hat{U}_r = \frac{U_r}{|\bar{U}_{r,i}|},$$

$$\hat{U}_z = \frac{U_z}{|\bar{U}_{r,i}|} \frac{r_i}{b}, \quad \hat{p} = \frac{p}{\rho \bar{U}_{\theta,i}^2} \quad (13)$$

The non-dimensional equations are as follows:

$$\frac{1}{\hat{r}} \frac{\partial(\hat{r}\hat{U}_r)}{\partial\hat{r}} + \frac{1}{(\gamma \tan \alpha)\hat{r}} \frac{\partial\hat{U}_\theta}{\partial\theta} + \frac{\partial\hat{U}_z}{\partial\hat{z}} = 0 \quad (14)$$

$$\hat{U}_r \frac{\partial\hat{U}_r}{\partial\hat{r}} + \frac{\hat{U}_\theta}{(\gamma \tan \alpha)\hat{r}} \frac{\partial\hat{U}_r}{\partial\theta} + \hat{U}_z \frac{\partial\hat{U}_r}{\partial\hat{z}} - \frac{\hat{U}_\theta^2}{(\gamma \tan \alpha)^2 \hat{r}}$$

$$= -\frac{1}{(\tan \alpha)^2} \frac{\partial\hat{p}}{\partial\hat{r}} + \frac{1}{Ds} \left[ \frac{\partial^2\hat{U}_r}{\partial\hat{z}^2} + \frac{b^2}{r_i^2} \right]$$

$$\times \left( \frac{1}{\hat{r}^2} \frac{\partial^2\hat{U}_r}{\partial\theta^2} - \frac{2}{(\gamma \tan \alpha)\hat{r}^2} \frac{\partial\hat{U}_\theta}{\partial\theta} + \frac{1}{\hat{r}} \frac{\partial}{\partial\hat{r}} \left( \hat{r} \frac{\partial\hat{U}_r}{\partial\hat{r}} \right) - \frac{\hat{U}_r}{\hat{r}^2} \right) \quad (15)$$

$$\hat{U}_r \frac{\partial\hat{U}_\theta}{\partial\hat{r}} + \frac{\hat{U}_\theta}{(\gamma \tan \alpha)\hat{r}} \frac{\partial\hat{U}_\theta}{\partial\theta} + \hat{U}_z \frac{\partial\hat{U}_\theta}{\partial\hat{z}} + \frac{\hat{U}_r\hat{U}_\theta}{\hat{r}}$$

$$= -\frac{\gamma}{(\tan \alpha)\hat{r}} \frac{\partial\hat{p}}{\partial\theta} + \frac{1}{Ds} \left[ \frac{\partial^2\hat{U}_\theta}{\partial\hat{z}^2} + \frac{b^2}{r_i^2} \right]$$

$$\times \left( \frac{1}{\hat{r}^2} \frac{\partial^2\hat{U}_\theta}{\partial\theta^2} + \frac{2\gamma \tan \alpha}{\hat{r}^2} \frac{\partial\hat{U}_r}{\partial\theta} + \frac{1}{\hat{r}} \frac{\partial}{\partial\hat{r}} \left( \hat{r} \frac{\partial\hat{U}_\theta}{\partial\hat{r}} \right) - \frac{\hat{U}_\theta}{\hat{r}^2} \right) \quad (16)$$

$$\hat{U}_r \frac{\partial\hat{U}_z}{\partial\hat{r}} + \frac{\hat{U}_\theta}{(\gamma \tan \alpha)\hat{r}} \frac{\partial\hat{U}_z}{\partial\theta} + \hat{U}_z \frac{\partial\hat{U}_z}{\partial\hat{z}}$$

$$= -\frac{r_i^2}{b^2(\tan \alpha)^2} \left( \frac{\partial\hat{p}'}{\partial\hat{z}} \right)$$

$$+ \frac{1}{Ds} \left[ \frac{b^2}{r_i^2} \left( \frac{1}{\hat{r}} \frac{\partial}{\partial\hat{r}} \left( \hat{r} \frac{\partial\hat{U}_z}{\partial\hat{r}} \right) + \frac{1}{\hat{r}^2} \frac{\partial^2\hat{U}_z}{\partial\theta^2} \right) + \frac{\partial^2\hat{U}_z}{\partial\hat{z}^2} \right] \quad (17)$$

[In equation (17),  $p'$  is the modified pressure which is equal to  $(p - \rho g_z z)$  and  $g_r$  and  $g_\theta$  are considered to be zero.]

Equations (14) to (17) can be solved for the boundary conditions given below.

$$\text{at } \hat{z} = 0 \text{ and } 1, \quad \hat{U}_r = 0, \quad \hat{U}_\theta = \hat{r}, \quad \hat{U}_z = 0 \quad (18)$$

$$\text{at } \hat{r} = 1, \quad \hat{U}_r = \hat{U}_{r,i}, \quad \hat{U}_\theta = \hat{U}_{\theta,i}, \quad \hat{U}_z = 0 \quad (19)$$

$$\text{at } \hat{r} = \frac{r_o}{r_i}, \quad \hat{p} = 0 \quad (20)$$

Equation (19) is written on the basis of the assumption that the flow rate is uniform throughout the periphery of the inlet plane. This condition can be achieved for a Tesla turbine either by increasing the number of nozzles at rotor inlet or by using a plenum chamber at rotor inlet (which is found in the design of a Tesla disc turbine given by Lemma et al.<sup>6</sup>).

### Application of the principle of similitude CFD simulation

A commercially available CFD software Fluent 6.3.26 is utilized for the present computation. Three-dimensional, double precision, pressure based, steady and implicit solver is used. Velocity formulation is in the absolute frame of reference and flow is considered to be laminar. The SIMPLE algorithm, with upwind scheme for momentum and 'standard' scheme for discretizing the pressure equation, is utilized. Under-relaxation factors for momentum, pressure, density, and body force are chosen, respectively, 0.7, 0.3, 1 and 1.

The geometry and the computational grid are generated by the commercially available software GAMBIT 2.4.6. Two successive discs, separated by a small gap ( $b$ ), are considered as the domain for the present CFD analysis. Each disc has an inlet radius ( $r_i$ ) and an outlet radius ( $r_o$ ). The results of CFD simulations have been presented for two widely different values of radius ratio  $\hat{r}_o$  which are 0.528 (corresponding to  $r_i = 25$  mm and  $r_o = 13.2$  mm) and 0.2 (corresponding to  $r_i = 25$  mm and  $r_o = 5$  mm). Absolute tangential velocity ( $\bar{U}_{\theta,i}$ ), radial velocity ( $\bar{U}_{r,i}$ ) and  $z$  component of velocity ( $U_z$ ) are specified at the inlet (for the present study,  $\bar{U}_{\theta,i} \neq 0$ ,  $\bar{U}_{r,i} \neq 0$  and  $U_{z,i} = 0$ ). Outlet boundary condition at the exit is modelled as pressure outlet with zero gauge pressure. No slip boundary condition is set on the disc walls. A rotational speed ( $\Omega$ ) of the disc is also set. Air is used as a working fluid for the CFD simulations of the prototype.

In order to systematically select an appropriate convergence criterion, the flow for the same computational domain has been simulated thrice as the maximum residual is set respectively at  $10^{-9}$ ,  $10^{-10}$  and  $10^{-11}$ . It is found that when the maximum residual is changed from  $10^{-10}$  to  $10^{-11}$ , the corresponding change in  $\Delta p_{io}$  is less than  $10^{-5}\%$ . Hence, a maximum residual of  $10^{-10}$  is chosen as the convergence criterion for the present study.

A grid-independence test has been carried out (Table 1 showing a few pertinent details), and based on this study, a total of 1,140,000 ( $60 \times 190 \times 100$ ) mapped, hexahedral computational cells are used for  $\hat{r}_o = 0.528$  (for  $\hat{r}_o = 0.2$ , a total of 2,280,000 ( $60 \times 190 \times 200$ ) cells are used). Among several output parameters,  $\Delta p_{io}$ , for its relatively high sensitivity with the change in the number of computational

**Table 1.** Grid-independence test (for  $r_i = 0.025$  m,  $r_o = 0.0132$  m,  $b = 10^{-4}$  m,  $\Omega = 1000$  rad/s,  $\hat{U}_{r,i} = -11.5$  m/s,  $\hat{U}_{\theta,i} = 106$  m/s,  $U_{z,i} = 0$  m/s, velocity profiles are uniform at inlet, air is used as working fluid).

Grid distribution	Number of grids in $r, \theta$ and $z$ directions	Total number of cells	$\Delta p_{io}$ (Pa)
Coarse	(50 × 95 × 30)	142,500	5005
Standard	(100 × 190 × 60)	1,140,000	5021
Fine	(150 × 285 × 90)	3,847,500	5020

cells, is chosen as a testing parameter to determine the optimum number of cells. Table 1 shows the computed values of  $\Delta p_{io}$  for three different grid distributions (coarse, standard and fine). While increasing the number of cells simultaneously in the  $r, \theta$  and  $z$  directions, it has been observed that, the computed value of  $\Delta p_{io}$  varies until a grid distribution of  $100 \times 190 \times 60$ , which corresponds to a total of 1,140,000 computational cells, is attained. However, any further increase in the number of computational cells in the  $r, \theta$  and  $z$  directions leads to a marginal change of  $\Delta p_{io}$  (e.g. the computed value of  $\Delta p_{io}$  for 3,847,500 cells differs marginally from the computed value of  $\Delta p_{io}$  for 1,140,000 cells; see Table 1).

The validation of the numerical results has been discussed by Sengupta and Guha.<sup>25</sup> These issues are therefore not described here for the sake of brevity and for keeping the discussion focussed.

Figure 2 shows the contours of non-dimensional velocities on a  $rz$  plane for  $\hat{r}_o = 0.2$ . Figures 2a and 2b show, respectively, contours of the non-dimensional absolute and relative tangential velocities. Figure 2c shows a contour of the absolute value (modulus) of non-dimensional radial velocity.

For no slip boundary condition on the surface of both discs ( $\hat{z} = 0$  and  $\hat{z} = 1$ ), the non-dimensional relative tangential velocity  $\hat{V}_\theta (= V_\theta/(\Omega r_i))$  in Figure 2a and the modulus of non-dimensional radial velocity  $|\hat{U}_r| (= |U_r/\hat{U}_{r,i}|)$  in Figure 2c are zero, and, the non-dimensional absolute tangential velocity  $\hat{U}_\theta (= U_\theta/(\Omega r_i))$  in Figure 2b is equal to the non-dimensional radius  $\hat{r}$ . Figure 2 shows that  $\hat{V}_\theta, \hat{U}_\theta$  and  $|\hat{U}_r|$  gradually increase from the disc-surfaces ( $\hat{z} = 0$  and  $\hat{z} = 1$ ) and obtain a maximum value at the middle of the disc spacing ( $\hat{z} = 1/2$ ).

Figure 2 also shows the  $r$ -variation of  $\hat{V}_\theta, \hat{U}_\theta$  and  $|\hat{U}_r|$ . It can be seen from Figure 2a that, with decreasing  $\hat{r}$  from  $\hat{r} = 1$  (inlet),  $\hat{V}_\theta$  decreases to a minimum at a certain radius and then onwards increases. It can be shown from equation (1) that  $\hat{U}_\theta$  depends on  $\hat{V}_\theta$  and  $\hat{r}$ .  $\hat{r}$  decreases as one moves from the inlet ( $\hat{r} = 1$ ) to the outlet ( $\hat{r} = r_o/r_i$ ). It can be observed from Figure 2b that  $\hat{U}_\theta$  decreases rapidly at the region where  $\hat{V}_\theta$  decreases. This region is near the inlet. With further decrease of  $\hat{r}$ , Figure 2b shows a region where  $\hat{U}_\theta$  varies slowly. In this region, the effect of increase in

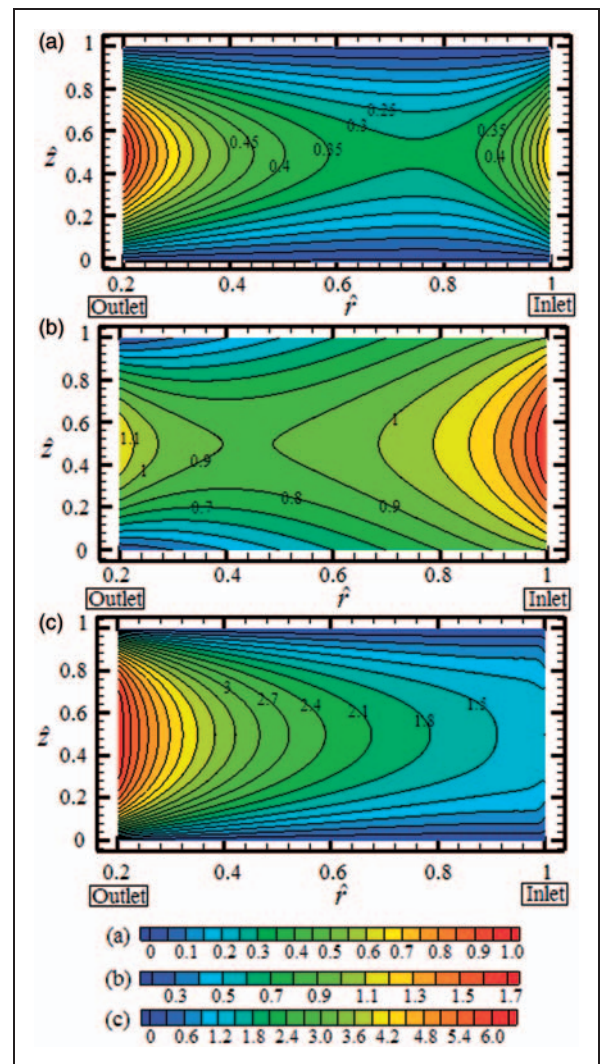


**Figure 2.** Contour of non-dimensional velocities on a  $rz$  plane. (a) Contour of  $\hat{V}_\theta$ ; (b) contour of  $\hat{U}_\theta$ ; (c) contour of  $|\hat{U}_r|$ . (Results obtained from CFD simulation for  $\hat{r}_o = 0.2$ ,  $\hat{b} = 0.0058$ ,  $\gamma = 1.462$ ,  $\alpha = 6.2^\circ$ ,  $Ds = 0.66$  and parabolic velocity distribution at inlet.). A color version of this figure is available in online.

$\hat{V}_\theta$  opposes and suppresses the effect of decrease in  $\hat{r}$ . Near outlet, the effect of increase in  $\hat{V}_\theta$  dominates over the effect of decrease in  $\hat{r}$ . Figure 2b shows that  $\hat{U}_\theta$  increases near outlet. Figure 2c shows that  $|\hat{U}_r|$  progressively increases in the  $r$  direction towards

outlet. It is so because the flow area ( $2\pi rb$ ) decreases with a decrease in  $\hat{r}$  and the fluid flow (steady, incompressible and axi-symmetric) has to satisfy the equation of continuity.

### Example calculations demonstrating the principle of similitude

In this section, the similarity between the model and prototype has been demonstrated with example calculations. The aspect ratio ( $\hat{b}$ ), radius ratio ( $\hat{r}_o$ ), tangential speed ratio at inlet ( $\gamma$ ), flow angle at inlet ( $\alpha$ ) and dynamic similarity number ( $Ds$ ) of the model should be same as those of the prototype to achieve geometric, kinematic and dynamic similarity simultaneously. The geometrical and operational details of the model and prototype used in the example calculations have been provided in Table 2. The calculations are performed for both uniform and parabolic inlet velocity distributions.

**Example calculation 1.** As the first example, variation of geometry is considered while keeping the same fluid. Let us consider a case when the value of  $b$  for the model (denoted as  $b_m$ ) is twice than that of the prototype (denoted as  $b_p$ ). Therefore,  $b_m/b_p = 2$ .

Geometric similarity is ensured by keeping the value of  $b/r_i$  and  $r_o/r_i$  of the model same as that of the prototype. Hence,  $(r_i)_m/(r_i)_p = 2$  and  $(r_o)_m/(r_o)_p = 2$ .

After achieving geometric similarity,  $Ds$ ,  $\alpha$  and  $\gamma$  of the model need to be equal with those of the prototype to ensure complete dynamic similarity between the model and the prototype. The condition which

is required for  $Ds$  of the model to be equal with  $Ds$  of the prototype is  $(\bar{U}_{r,i})_m/(\bar{U}_{r,i})_p = 1/2$ .

Constancy of  $\alpha$  requires  $(\bar{U}_{\theta,i})_m/(\bar{U}_{\theta,i})_p = 1/2$ .

Moreover, the additional condition which is needed for equalizing  $\gamma$  of the model to that of the prototype is  $\Omega_m/\Omega_p = 1/4$ .

**Example calculation 2.** Now, consider a separate case when the geometry of the model is the same as that of the prototype; however, the kinematic viscosity of the working fluid used in case of the model is half as that for the case of the prototype. Hence, to conserve the value of  $Ds$  one needs the following condition  $(\bar{U}_{r,i})_m/(\bar{U}_{r,i})_p = 1/2$ .

Additionally, to conserve  $\alpha$  one needs  $(\bar{U}_{\theta,i})_m/(\bar{U}_{\theta,i})_p = 1/2$ .

Also to maintain a fixed value of  $\gamma$  one further needs  $\Omega_m/\Omega_p = 1/2$ .

**Observations.** Table 2 shows the results of the example calculations performed for both uniform and parabolic velocity distributions at inlet. It can be observed from Table 2 that for both cases the power coefficient ( $\hat{W}$ ) and the pressure-drop coefficient ( $\Delta\hat{p}_{io}$ ) of the models (calculated by three-dimensional CFD) are exactly equal to those of the prototype (also calculated by three-dimensional CFD). Hence, the principle of similitude is demonstrated.

Figure 3 shows the  $z$ -variation of the non-dimensional  $z$ -velocity  $\hat{U}_z$  at a particular non-dimensional radius  $\hat{r} = 0.8$  for the prototype and its models. The results obtained from three separate CFD simulations are found to be exactly superposed on one another.

**Table 2.** Values of input and output parameters of CFD simulations.

	Similitude example 1		Similitude example 2	
	Model 1	Prototype	Model 2	Prototype
$b$ (m)	$2 \times 10^{-4}$	$10^{-4}$	$10^{-4}$	$10^{-4}$
$r_i$ (m)	0.05	0.025	0.025	0.025
$r_o$ (m)	0.0264	0.0132	0.0132	0.0132
$\bar{U}_{r,i}$ (m/s)	-5.75	-11.5	-5.75	-11.5
$\bar{U}_{\theta,i}$ (m/s)	53	106	53	106
$\Omega$ (rad/s)	250	1000	500	1000
$\nu$ (m <sup>2</sup> /s)	$1.46 \times 10^{-5}$	$1.46 \times 10^{-5}$	$0.73 \times 10^{-5}$	$1.46 \times 10^{-5}$
Uniform velocity distribution at inlet	$\frac{\dot{W}}{\rho \bar{U}_{r,i} ^3 r_i^2}$	0.46	0.46	0.46
	$\frac{\Delta p_{io}}{\rho\bar{U}_{\theta,i}^2}$	0.36	0.36	0.36
Parabolic velocity distribution at inlet	$\frac{\dot{W}}{\rho \bar{U}_{r,i} ^3 r_i^2}$	0.54	0.54	0.54
	$\frac{\Delta p_{io}}{\rho\bar{U}_{\theta,i}^2}$	0.37	0.37	0.37

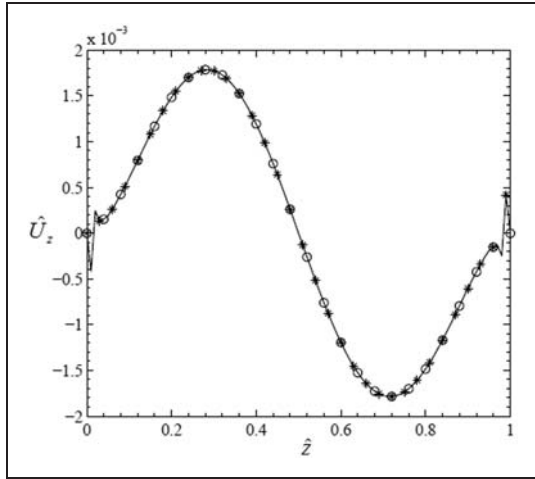


**Figure 3.** Variation of  $\hat{U}_z$  at a particular radial location ( $\hat{r} = 0.8$ ): results obtained from CFD simulation. (Keys: —●— Prototype, - \* - Model 1, - ◻ - Model 2. All calculations have been performed for parabolic velocity distribution at inlet.)

This equality of the values of the non-dimensional  $z$ -velocity demonstrates the principle of similitude in the same way the equality of the power coefficient and the pressure-drop coefficient does so. However, the equality of the values of the non-dimensional  $z$ -velocity is perhaps more impressive when one considers the fact that the only physical boundary condition applied is  $U_z = 0$  at the inlet and on disc surfaces. The fact that such non-zero values of  $\hat{U}_z$  are evolved in the various cases of CFD simulation that the principle of similitude is exactly preserved indeed is a powerful evidence of the correctness of the dimensional analysis formulated in the present paper.

### Simplification of the non-dimensional conservation equations

In this section, a systematic method for arriving at simplified conservation equations of a Tesla turbine is presented. The geometry and operational details for the present simulations are the same as that of the prototype shown in Table 2. CFD simulations reveal that, for axi-symmetric boundary conditions, all three components ( $U_r$ ,  $U_\theta$  and  $U_z$ ) of velocity along with the pressure can be assumed axi-symmetric throughout the flow field. The non-dimensional conservation equations (14) to (17), simplified by the assumption of axi-symmetry, are given below.

$$\frac{1}{\hat{r}} \frac{\partial(\hat{r}\hat{U}_r)}{\partial\hat{r}} + \frac{\partial\hat{U}_z}{\partial\hat{z}} = 0 \tag{21}$$

$$\begin{aligned} \hat{U}_r \frac{\partial\hat{U}_r}{\partial\hat{r}} + \hat{U}_z \frac{\partial\hat{U}_r}{\partial\hat{z}} - \frac{\hat{U}_\theta^2}{\hat{r}(\gamma \tan \alpha)^2} \\ = -\frac{1}{(\tan \alpha)^2} \frac{\partial\hat{p}}{\partial\hat{r}} + \frac{1}{Ds} \left[ \frac{\partial^2\hat{U}_r}{\partial\hat{z}^2} + \frac{b^2}{r_i^2} \left( \frac{1}{\hat{r}} \frac{\partial}{\partial\hat{r}} \left( \hat{r} \frac{\partial\hat{U}_r}{\partial\hat{r}} \right) - \frac{\hat{U}_r}{\hat{r}^2} \right) \right] \end{aligned} \tag{22}$$

$$\begin{aligned} \hat{U}_r \frac{\partial\hat{U}_\theta}{\partial\hat{r}} + \hat{U}_z \frac{\partial\hat{U}_\theta}{\partial\hat{z}} + \frac{\hat{U}_r\hat{U}_\theta}{\hat{r}} \\ = \frac{1}{Ds} \left[ \frac{\partial^2\hat{U}_\theta}{\partial\hat{z}^2} + \frac{b^2}{r_i^2} \left( \frac{1}{\hat{r}} \frac{\partial}{\partial\hat{r}} \left( \hat{r} \frac{\partial\hat{U}_\theta}{\partial\hat{r}} \right) - \frac{\hat{U}_\theta}{\hat{r}^2} \right) \right] \end{aligned} \tag{23}$$

$$\begin{aligned} \hat{U}_r \frac{\partial\hat{U}_z}{\partial\hat{r}} + \hat{U}_z \frac{\partial\hat{U}_z}{\partial\hat{z}} = -\frac{r_i^2}{b^2(\tan \alpha)^2} \left( \frac{\partial\hat{p}'}{\partial\hat{z}} \right) \\ + \frac{1}{Ds} \left[ \frac{b^2}{r_i^2} \left( \frac{1}{\hat{r}} \frac{\partial}{\partial\hat{r}} \left( \hat{r} \frac{\partial\hat{U}_z}{\partial\hat{r}} \right) \right) + \frac{\partial^2\hat{U}_z}{\partial\hat{z}^2} \right] \end{aligned} \tag{24}$$

The term  $b/r_i$  ( $\hat{b}$ ) is small for all practical Tesla disc turbines and therefore the terms associated with  $\hat{b}^2$  and  $\hat{b}^4$  are neglected. Hence, equations (22) to (24) can be further simplified as follows:

$$\hat{U}_r \frac{\partial\hat{U}_r}{\partial\hat{r}} + \hat{U}_z \frac{\partial\hat{U}_r}{\partial\hat{z}} - \frac{\hat{U}_\theta^2}{\hat{r}(\gamma \tan \alpha)^2} = -\frac{1}{(\tan \alpha)^2} \frac{\partial\hat{p}}{\partial\hat{r}} + \frac{1}{Ds} \frac{\partial^2\hat{U}_r}{\partial\hat{z}^2} \tag{25}$$

$$\hat{U}_r \frac{\partial\hat{U}_\theta}{\partial\hat{r}} + \hat{U}_z \frac{\partial\hat{U}_\theta}{\partial\hat{z}} + \frac{\hat{U}_r\hat{U}_\theta}{\hat{r}} = \frac{1}{Ds} \frac{\partial^2\hat{U}_\theta}{\partial\hat{z}^2} \tag{26}$$

$$\frac{\partial\hat{p}'}{\partial\hat{z}} = 0 \tag{27}$$

When  $\hat{b}$  is small and  $\hat{r}_o$  is not small, a further simplification is possible. CFD simulations presented in Figure 3 show that, under such conditions, the order of magnitude of  $\hat{U}_z$  is very small ( $10^{-3}$  for the example calculations). Therefore, equation (21) and equations (25) to (27) can be further simplified as follows.

$$\frac{1}{\hat{r}} \frac{\partial(\hat{r}\hat{U}_r)}{\partial\hat{r}} = 0 \tag{28}$$

$$(\tan \alpha)^2 \hat{U}_r \frac{\partial\hat{U}_r}{\partial\hat{r}} - \frac{1}{\gamma^2} \frac{\hat{U}_\theta^2}{\hat{r}} = -\frac{d\hat{p}}{d\hat{r}} + \frac{(\tan \alpha)^2}{Ds} \frac{\partial^2\hat{U}_r}{\partial\hat{z}^2} \tag{29}$$

$$\hat{U}_r \frac{\partial\hat{U}_\theta}{\partial\hat{r}} + \frac{\hat{U}_r\hat{U}_\theta}{\hat{r}} = \frac{1}{Ds} \frac{\partial^2\hat{U}_\theta}{\partial\hat{z}^2} \tag{30}$$

Sengupta and Guha<sup>11</sup> have given a closed-form analytical solution of equations (28) to (30) by transforming the absolute velocity components into the relative frame of reference. A deeper understanding of Figure 2 may be obtained with the help of this simple analytical theory.

According to the prediction of this analytical theory, the variation of the area-averaged non-dimensional

relative tangential velocity  $\hat{V}_\theta$  along the radial direction is:

$$\hat{V}_\theta = \bar{V}_\theta / \Omega r_i = (\gamma - 1) \times \left[ \frac{C_2 / C_1 + (1 - C_2 / C_1) \exp\{C_1(1 - \hat{r}^2)/2\}}{\hat{r}} \right]$$

where

$$C_1 = \frac{10}{Ds}, \quad C_2 = \frac{-10}{6(\gamma - 1)} \quad (31)$$

The expression for the non-dimensional number  $C_1$  was written in terms of several dimensional variables in Sengupta and Guha.<sup>11</sup> Here, we have established the connection between  $C_1$  and  $Ds$  giving further physical insight.

Equation (31) shows that the variation of  $\hat{V}_\theta$  along the radial direction depends on the values of  $Ds$  and  $\gamma$ . Hence, the predictions, which are inferred from Figures 2a and 2b, are not universal. Guha and Sengupta<sup>12</sup> had shown that the variation of area-averaged relative tangential velocity along radial direction depends on inertial, viscous and Coriolis forces. The relative magnitude of inertial, viscous and Coriolis forces at any radius will vary with the change in  $Ds$  and  $\gamma$ .

According to the analytical theory, the closed-form expression for torque produced by one side of a single disc of a Tesla turbine is as follows:

$$\Gamma = \frac{12\pi\mu\bar{V}_{\theta,i}r_i^3}{b} \left[ \frac{-Ds}{12(\gamma - 1)}(1 - \hat{r}_o^2) - \frac{Ds}{10} \times \left( 1 + \frac{Ds}{6(\gamma - 1)} \right) \left\{ 1 - \exp\left[ \frac{5}{Ds}(1 - \hat{r}_o^2) \right] \right\} \right] \quad (32)$$

The power coefficient due to viscous drag for the fluid flow between two successive discs can be expressed as  $\hat{W} = 2\Gamma\Omega/(\rho|\bar{U}_{r,i}|^3r_i^2)$ . In reality, a Tesla turbine consists of multiple discs. The total

power coefficient of a rotor consisting of  $n$  discs is given by:

$$\hat{W} = \frac{2(n - 1)\Gamma\Omega}{\rho|\bar{U}_{r,i}|^3r_i^2} \quad (33)$$

The power coefficients for various values of  $\gamma$ , calculated both by CFD and the analytical relation, are given in Table 3. The geometry and inlet velocity components for all calculations are same as that of the prototype given in Table 2, and parabolic velocity distributions are considered at inlet. It can be seen that the power coefficients calculated from the analytical expressions (equations (32) and (33)) match well with those obtained from the CFD simulations, particularly when second order upwind scheme is used.

The variation of power output and pressure drop for two similar models (such as Model A and Model B, whose descriptions are given in Table 4) with the variation of rotational speed of the discs can be predicted by solving equations (28) to (30) using the analytical method developed by Sengupta and Guha.<sup>11</sup> In order to set a critical test for the principle of similitude developed in the present work, Model A and Model B are chosen to differ simultaneously in geometry, operating flow conditions and the working fluid. Each of the curves shown in Figures 4a and 4b contains many data points. If each data point were to be calculated by making a complete run of the CFD code up to convergence, then the total computational time would be very large. Thus the analytical theory (equations (28) to (30)) has been used. Figures 4a and 4b show the dimensional representation of the relevant parameters applicable for Model A and Model B respectively.  $\Delta p_{io}$ , in Figure 4a, increases from 4565 Pa to 26,119 Pa corresponding to an increase of  $\Omega$  from 424 rad/s to 8480 rad/s; and,  $\Delta p_{io}$ , in Figure 4b, increases from 7776 Pa to 44,491 Pa corresponding to an increase of  $\Omega$  from 13 rad/s to 258 rad/s. Both figures show that, with an increase in  $\Omega$ ,  $\dot{W}$  increases until  $\dot{W}$  obtains a maximum value, and, any further increase of  $\Omega$  leads to a decrease of  $\dot{W}$ . The maximum value of  $\dot{W}$  in Figure 4a is 1.7 W and it

**Table 3.** Comparison between the analytical results and the results obtained from CFD simulations.\*

Tangential speed ratio at inlet ( $\gamma$ )	$\dot{W}/(\rho \bar{U}_{r,i} ^3r_i^2)$ from analytical expression (equations (32) and (33))	$\dot{W}/(\rho \bar{U}_{r,i} ^3r_i^2)$ from CFD simulation (using 1st order upwind scheme)	$\dot{W}/(\rho \bar{U}_{r,i} ^3r_i^2)$ from CFD simulation (using 2nd order upwind scheme)
4.24	0.54	0.53	0.54
1.696	1.10	1.07	1.10
0.848	1.40	1.20	1.38

\*Values of all input parameters except  $\Omega$  are the same as those for the prototype given in Table 2. For all calculations parabolic velocity distribution is considered at inlet.

**Table 4.** Geometric details and operating parameters for two similar models.

Parameters	Model A	Model B
$b$ (m)	0.0001	0.00015
$r_i$ (m)	0.025	0.0375
$r_o$ (m)	0.0132	0.0198
Working fluid	Air	Water
$\rho$ (kg/m <sup>3</sup> )	1.225	998.2
$\mu$ (kg/ms)	1.7894e-05	0.001
$\bar{U}_{r,i}$ (m/s)	-11.5	$-11.5(b_A/b_B)(v_B/v_A) = -0.53$
$\bar{U}_{\theta,i}$ (m/s)	106	$106(b_A/b_B)(v_B/v_A) = 4.85$

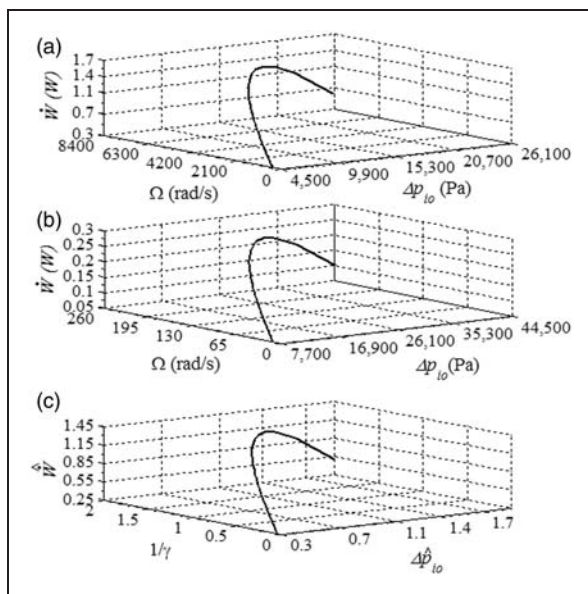


**Figure 4.** Dimensional and non-dimensional representations of the variations of power output and pressure drop with the rotational speed of the discs for two similar models. (a) Dimensional representation for Model A; (b) Dimensional representation for Model B; (c) Non-dimensional representation applicable for both Model A and Model B. (Descriptions of the models are given in Table 4.)

is obtained for  $\Omega = 4711$  rad/s whereas, the maximum value of  $\dot{W}$  in Figure 4b is 0.3 W and it is obtained for  $\Omega = 144$  rad/s. Figures 4c shows that the widely different dimensional data given in Figures 4a and 4b collapse into the same non-dimensional representation, demonstrating the validity of the criteria for similitude of Tesla disc turbines developed here.

**Conclusion**

A dimensional analysis for the three-dimensional rotating flow within the narrow spacing of multiple concentric discs is presented. The analysis has three important outcomes.

First of all, the present analysis provides the appropriate non-dimensional numbers by which the flow physics of the rotating flow within the narrow spacing of multiple concentric discs can be explained and quantified. The criteria for achieving geometric, kinematic and dynamic similarity between a model and the prototype have been established. The principle of similitude has been demonstrated analytically as well as through many three-dimensional CFD simulations. Seven non-dimensional numbers of importance have been identified for a Tesla disc turbine: (i) radius ratio:  $\hat{r}_o = r_o/r_i$ , (ii) aspect ratio:  $\hat{b} = b/r_i$ , (iii) tangential speed ratio at inlet:  $\gamma = \bar{U}_{\theta,i}/(\Omega r_i)$ , (iv) flow angle at inlet:  $\alpha = \tan^{-1}(|\bar{U}_{r,i}|/\bar{U}_{\theta,i})$  (which is same as the nozzle angle), (v) dynamic similarity number:  $Ds = (b/r_i)(|\bar{U}_{r,i}|b/\nu)$ , (vi) power coefficient:  $\hat{W} = \dot{W}/(\rho|\bar{U}_{r,i}|^3 r_i^2)$ , and (vii) pressure-drop coefficient:  $\Delta \hat{p}_{io} = \Delta p_{io}/(\rho \bar{U}_{\theta,i}^2)$ . Geometric similarity is ensured by keeping the value of  $\hat{r}_o$  and  $\hat{b}$  of the model same as that of the prototype. After achieving geometric similarity,  $Ds$ ,  $\alpha$  and  $\gamma$  of the model need to be equal with those of the prototype to ensure complete dynamic similarity between the model and the prototype. For a Tesla disc compressor (or pump), a similar analysis is applicable if two non-dimensional numbers are suitably modified: a flow coefficient  $\phi$  ( $\phi \equiv |\bar{U}_{r,i}|/\Omega r_i$ ) may be used instead of  $\alpha$ , and, the Pohlhausen number ( $\Omega b^2/\nu$ ) may be used instead of the dynamic similarity number  $Ds$  formulated here (the name “dynamic similarity number” is coined in this work).

The second important outcome of the present work is that the analysis leads to proper scaling laws. These can directly be used, for example, to design an efficient Tesla disc turbine under any particular working condition. The performance and efficiency of Tesla turbines with various length scales and operating conditions can thus be theoretically assessed before manufacturing or experimentation. For a prototype and a dynamically similar model, the power coefficient and the pressure-drop coefficient remain the same. The formula for power coefficient given above may also be interpreted to mean that the power of dynamically similar Tesla disc turbines would also scale with  $\rho \Omega^3 b^5$ . Similarly, the pressure-drop of dynamically similar Tesla disc turbines would also scale with  $\rho \Omega^2 b^2$ .

Thirdly, the conservation equations can be simplified depending on the relative magnitudes of some of the non-dimensional numbers. Such simplification makes it possible to arrive at a closed-form analytical solution for the three-dimensional flow field within a Tesla disc turbine.

**Funding**

This research received no specific grant from any funding agency in the public, commercial, or not-for-profit sectors.

## References

1. Dixon SL and Hall CA. *Fluid Mechanics and Thermodynamics of Turbomachinery*. 6th ed, Elsevier Inc, New Delhi, India, 2012.
2. Tesla N. *Turbine*. US patent 1061206, 1913.
3. Guha A. Optimisation of aero gas turbine engines. *Aeronaut J* 2001; 105(1049): 345–358.
4. Guha A. Performance and optimization of gas turbines with real gas effects. *Proceedings of the Institution of Mechanical Engineers, Part A: Journal of Power and Energy* 2001; 215(4): 507–512.
5. Rice W. Tesla turbomachinery. In: E Logan (ed.) *Handbook of turbomachinery*. New York: Marcel Dekker, 2003, pp.861–874.
6. Lemma E, Deam RT, Toncich D, et al. Characterisation of a small viscous flow turbine. *J Exp Thermal Fluid Sci* 2008; 33: 96–105.
7. Hoya GP and Guha A. The design of a test rig and study of the performance and efficiency of a Tesla disc turbine. *Proceedings of the Institution of Mechanical Engineers, Part A: Journal of Power and Energy* 2009; 223(A4): 451–465.
8. Guha A and Smiley B. Experiment and analysis for an improved design of the inlet and nozzle in Tesla disc turbines. *Proceedings of the Institution of Mechanical Engineers, Part A: Journal of Power and Energy* 2010; 224: 261–277.
9. Rice W. An analytical and experimental investigation of multiple-disk turbines. *ASME Trans J Eng Power* 1965; 87(1): 29–36.
10. Carey VP. Assessment of Tesla turbine performance for small scale solar Rankine combined heat and power systems. *ASME Trans J Eng Gas Turbines Power* 2010; 132(12): 122301.
11. Sengupta S and Guha A. A theory of Tesla disc turbines. *Proceedings of the Institution of Mechanical Engineers, Part A: Journal of Power and Energy* 2012; 226(5): 650–663.
12. Guha A and Sengupta S. The fluid dynamics of the rotating flow in a Tesla disc turbine. *Eur J Mech B/Fluids* 2013; 37: 112–123.
13. Shevchuk IV. *Convective heat and mass transfer in rotating disk systems*. Berlin, Heidelberg: Springer Verlag, 2009.
14. Batchelor GK. Note on a class of solutions of the Navier-Stokes equations representing steady rotationally-symmetric flow. *Quat J Mech Appl Math* 1951; 4: 29–41.
15. Guha A. Jump conditions across normal shock waves in pure vapour-droplet flows. *J Fluid Mech* 1992; 241: 349–369.
16. Guha A. A unified theory of aerodynamic and condensation shock waves in vapour-droplet flows with or without a carrier gas. *Phys Fluids* 1994; 6(5): 1893–1913.
17. Guha A. Computation, analysis and theory of two-phase flows. *Aeronaut J* 1998; 102(1012): 71–82.
18. Guha A. A unified theory for the interpretation of total pressure and temperature in two-phase flows at subsonic and supersonic speeds. *Proceedings of the Royal Society A: Mathematical, Physical and Engineering Sciences* 1998; 454: 671–695.
19. Guha A. A simple, analytical theory for interpreting measured total pressure in multiphase flows. *ASME J Fluids Eng* 1998; 120: 385–389.
20. Schmidt DD. *Biomass boundary layer turbine power system*. Energy Innovations Small Grant (EISG) Program, 2002.
21. Steidel R and Weiss H. *Performance test of a bladeless turbine for geothermal applications*. Lawrence Livermore Laboratory, Report No. UCID-17068, 1974.
22. Armstrong JH. *An investigation of the performance of a modified Tesla turbine*. MS Thesis, Georgia Institute of Technology, 1952.
23. Beans EW. Investigation into the performance characteristics of a friction turbine. *J Spacecraft* 1966; 3(1): 131–134.
24. Davydov AB and Sherstyuk AN. Experimental research on a microturbine. *Russian Eng J* 1980; 60(8): 26–28.
25. Sengupta S and Guha A. Analytical and computational solutions for three-dimensional flow-field and relative pathlines for the rotating flow in a Tesla disc turbine. *Comp Fluids* 2013; 88: 344–353.

## Appendix I

## Notation

$b$	gap between the two discs
$\hat{b}$	aspect ratio
$Ds$	dynamic similarity number
$p$	pressure
$p'$	modified pressure, $p' \equiv p - \rho g_z z$
$r$	radial direction in cylindrical co-ordinate system
$\hat{r}_o$	radius ratio
$U$	absolute velocity of fluid
$V$	relative velocity of fluid
$\dot{W}$	power output
$\hat{W}$	power coefficient, $\hat{W} \equiv \frac{\dot{W}}{(\rho  \bar{U}_{r,i} ^3 r_i^2)}$
$z$	$z$ direction in cylindrical co-ordinate system
$\alpha$	flow angle at inlet
$\Gamma$	torque produced by one side of a single disc
$\gamma$	tangential speed ratio at inlet, $\gamma \equiv \frac{\bar{U}_{\theta,i}}{\Omega r_i}$
$\Delta p_{io}$	pressure drop between inlet and outlet
$\Delta \hat{p}_{io}$	pressure-drop coefficient, $\Delta \hat{p}_{io} \equiv \Delta p_{io} / \rho \bar{U}_{\theta,i}^2$
$\theta$	Azimuthal direction in cylindrical co-ordinate system
$\mu$	viscosity of the working fluid
$\nu$	kinematic viscosity of working fluid
$\rho$	density of the working fluid
$\Omega$	rotational speed of the disc

## Subscripts

$i$	at rotor inlet
$m$	model

- $o$  at rotor outlet
- $p$  prototype
- $r$  component along the  $r$  direction
- $z$  component along the  $z$  direction
- $\theta$  component along the  $\theta$  direction

**Superscripts**

- $\bar{()}$  area-averaged flow variables
- $\hat{()}$  non-dimensional flow variables

**Appendix 2**

The functional relationship between the input variables ( $r_i, r_o, b, |\bar{U}_{r,i}|, \bar{U}_{\theta,i}, \Omega, \rho, \mu$ ) and the output variables ( $\dot{W}, \Delta p_{io}$ ) can be written as

$$F(r_i, r_o, b, |\bar{U}_{r,i}|, \bar{U}_{\theta,i}, \Omega, \rho, \mu, \dot{W}, \Delta p_{io}) = 0.$$

Table 5 shows the variables and their dimensions. In the present analysis,  $r_i, |\bar{U}_{r,i}|$  and  $\rho$  are selected as repeating variables. According to Buckingham Pi

1.  $\Pi_1 = r_i^{x_1} |\bar{U}_{r,i}|^{x_2} \rho^{x_3} \dot{W}$   
Solution of the algebraic equations gives  $x_1 = -2, x_2 = -3$  and  $x_3 = -1$   
Hence,  $\Pi_1 = \frac{\dot{W}}{\rho |\bar{U}_{r,i}|^3 r_i^2}$
2.  $\Pi_2 = r_i^{x_1} |\bar{U}_{r,i}|^{x_2} \rho^{x_3} r_o$   
Solution of the algebraic equations gives  $x_1 = -1, x_2 = 0$  and  $x_3 = 0$   
Hence,  $\Pi_2 = \frac{r_o}{r_i}$
3.  $\Pi_3 = r_i^{x_1} |\bar{U}_{r,i}|^{x_2} \rho^{x_3} b$   
Solution of the algebraic equations gives  $x_1 = -1, x_2 = 0$  and  $x_3 = 0$   
Hence,  $\Pi_3 = \frac{b}{r_i}$
4.  $\Pi_4 = r_i^{x_1} |\bar{U}_{r,i}|^{x_2} \rho^{x_3} \Delta p_{io}$   
Solution of the algebraic equations gives  $x_1 = 0, x_2 = -2$  and  $x_3 = -1$ .  
Hence,  $\Pi_4 = \frac{\Delta p_{io}}{\rho |\bar{U}_{r,i}|^2}$
5.  $\Pi_5 = r_i^{x_1} |\bar{U}_{r,i}|^{x_2} \rho^{x_3} \bar{U}_{\theta,i}$   
Solution of the algebraic equations gives  $x_1 = 0, x_2 = -1$  and  $x_3 = 0$ .

**Table 5.** List of the variables and their dimensions:

Variable	$\dot{W}$	$r_i$	$r_o$	$b$	$\Delta p_{io}$	$ \bar{U}_{r,i} $	$\bar{U}_{\theta,i}$	$\Omega$	$\rho$	$\mu$
Dimension	$ML^2T^{-3}$	$L$	$L$	$L$	$ML^{-1}T^{-2}$	$LT^{-1}$	$LT^{-1}$	$T^{-1}$	$ML^{-3}$	$ML^{-1}T^{-1}$

theorem, there will be  $(10 - 3) = 7$  independent dimensionless groups or Pi groups. A Pi group can be formed as

$$\Pi = r_i^{x_1} |\bar{U}_{r,i}|^{x_2} \rho^{x_3} X$$

where  $X$  is a non-repeating variable.

Substituting the dimension of each variable and equating the exponents of  $M, L$  and  $T$  individually to zero, one can get a set of algebraic equations.  $x_1, x_2$  and  $x_3$  can be found out by solving the set of algebraic equations. This procedure is followed to derive the Pi terms given below.

- Hence,  $\Pi_5 = \frac{\bar{U}_{\theta,i}}{|\bar{U}_{r,i}|}$
6.  $\Pi_6 = r_i^{x_1} |\bar{U}_{r,i}|^{x_2} \rho^{x_3} \Omega$   
Solution of the algebraic equations gives  $x_1 = 1, x_2 = -1$  and  $x_3 = 0$ .  
Hence,  $\Pi_6 = \frac{\Omega r_i}{|\bar{U}_{r,i}|}$
7.  $\Pi_7 = r_i^{x_1} |\bar{U}_{r,i}|^{x_2} \rho^{x_3} \mu$   
Solution of the algebraic equations gives  $x_1 = -1, x_2 = -1$  and  $x_3 = -1$ .  
Hence,  $\Pi_7 = \frac{\mu}{\rho |\bar{U}_{r,i}| r_i}$